Journal of Advanced Ceramics
先进陶瓷
ISSN 2226-4108
CN 10-1154/TQ
清华大学出版社 Tsinghua University Press
SciOpen

J Adv Ceram 2026, **15**: 9221351

https://doi.org/10.26599/JAC.2026.9221351

Research Article

Non-equimolar compositional design engineered thermal expansion coefficients and conductivities of *m*′-$RETaO_4$ (RE = Sc, Y, Tm, Ho, Dy, Gd) high-entropy ceramics

Bingyan Wu[1, 2], Guangrong Li[3, *], Lin Chen[1, 2, *], Jiankun Wang[1, 2, 4], Wei Pan[1], Jing Feng[1, 2, 4, *]

[1] *Faculty of Materials Science and Engineering, Kunming University of Science and Technology, Kunming 650093, China*

[2] *National-Local Joint Engineering Laboratory for Technology of Advanced Metallic Solidification Forming and Equipment, Kunming 650093, China*

[3] *State Key Laboratory for Mechanical Behavior of Materials, School of Materials Science and Engineering, Xi'an Jiaotong University, Xi'an 710049, China*

[4] *Southwest United Graduate School, Kunming 650092, China*

* Corresponding author.

E-mail address: G. Li, ligrong@xjtu.edu.cn;

L. Chen, 1106846650@qq.com;

J. Feng, jingfeng@kust.edu.cn

Just Accepted

Journal of Advanced Ceramics https://mc03.manuscriptcentral.com/jacer
Received: March 31, 2026; Revised: June 28, 2026; Accepted: July 13, 2026

©The Author(s) 2026

清華大學出版社 Tsinghua University Press | SciOpen

Abstract: Rare-earth tantalates $RETaO_4$ have been extensively investigated as thermal protective materials, but their applications as environmental barrier coatings (EBCs) for ceramic matrix composites (CMCs) are limited by their high thermal expansion coefficients (TECs≥9.0×10^{-6} K^{-1}). The high-entropy design provides a feasible route to tailor the thermal properties of $RETaO_4$; however, most reports focus on equimolar $RETaO_4$ HECs. In this study, a series of non-equimolar monoclinic-prime (*m*′) $RETaO_4$ HECs are designed and synthesized to clarify the composition-structure-property relationships. The non-equimolar design is used to regulate configurational complexity, polyhedral distortion, and lattice strain in *m*′-RETaO4 within the same *m*′ phase. Atomic-scale TEM and GPA characterizations reveal the associated local distortion and lattice strain. These observations link non-equimolar composition with local structural distortion and macroscopic thermal transport behavior. The lowest thermal conductivity reaches 1.52-2.68 $W\cdot m^{-1}\cdot K^{-1}$ at 25-900 °C, and is mainly associated with RE-site disorder, lattice strain, and polyhedral distortion. Polyhedral distortion also suppresses thermal expansion by restricting atomic anharmonic vibrations. Among the designed compositions, the optimized non-equimolar *m*′-$RETaO_4$ HECs $(Sc_{0.2}Y_{0.2}Tm_{0.2}Ho_{0.2}Dy_{0.1}Gd_{0.1})TaO_4$ exhibits the lowest TECs of 6.2×10^{-6} K^{-1} at 1500 °C, closer to SiC-based CMCs than the other compositions, indicating its potential as candidate EBCs. This work proposes that polyhedral distortion and lattice strain are important structural factors for tailoring the thermal properties of non-equimolar $RETaO_4$ HECs, providing guidance for the design of complex oxides.

Keywords: non-equimolar design; high-entropy ceramics; lattice distortion; disorders; EBCs

Just Accepted

1 Introduction

SiC ceramic matrix composites (CMCs) are characterized by a low density, high-temperature stability, and oxidation resistance, which makes them suitable for hot-section components of gas turbine blades [1-3]. However, in combustion environments containing water vapor and molten salt impurities, CMCs suffer from severe recession and corrosion [4, 5]. To address these issues, environmental barrier coatings (EBCs) are applied to isolate CMCs from aggressive environments, thereby improving their stability and service life [6-9]. Rare-earth tantalates $RETaO_4$ are considered as potential EBCs owing to their high melting points, excellent phase stability, and good corrosion resistance [10-14]. However, the mismatch in thermal expansion coefficients (TECs) between $RETaO_4$ and SiC-CMCs remains a critical limitation for their application. SiC-based CMCs generally exhibit TECs of approximately $3.9\text{-}5.6\times10^{-6}$ K^{-1} [15-18]; therefore, minimizing the TECs mismatch is essential to reduce thermal stresses and enhance coating durability.

$RETaO_4$ typically exists in three polymorphs: monoclinic-prime (*m*′) [19], monoclinic (*m*) [20], and tetragonal (*t*) phases [21]. Among them, *m*′-$RETaO_4$ exhibits the lowest TECs of $5.0\text{-}8.0\times10^{-6}\cdot K^{-1}$. High-entropy engineering provides an effective strategy to reduce the TECs of *m*′-$RETaO_4$, thereby reducing interfacial stress between $RETaO_4$ and CMCs. Furthermore, reducing thermal conductivity improves thermal insulation performance of EBCs, and it is important for the protection of CMCs [22, 23].

High-entropy ceramics (HECs), defined as solid solutions containing five or more principal cations, have emerged as an effective strategy for tailoring thermal properties of various ceramics [24-27]. The high-entropy effect introduces severe lattice distortion and mass fluctuation, thereby reducing thermal conductivity and TECs [28-31]. Most existing studies on HECs focused on equimolar compositions to maximize configurational entropy (S_{conf}), but higher entropy does not necessarily guarantee better performance [32-35]. Equimolar designs often obscure the individual contributions of constituent elements, particularly the strain effects induced by ionic radius mismatch [36]. In contrast,

Just Accepted

non-equimolar design allows the molar ratios of constituent elements to be adjusted, thereby providing a route to tune compositional disorder, lattice distortion, and thermophysical properties [37, 38]. This approach enables access to specific critical states of lattice distortion to minimize thermal conductivity and optimize TECs, but it remains largely unexplored in $RETaO_4$ ceramics.

Previous studies indicate that the phase stability and phase-transition behavior of $RETaO_4$ are closely related to the RE^{3+} ionic radius, and the ionic-radius range around 0.100-0.102 nm can be regarded as a reference point for the phase transition of $RETaO_4$ [39-41]. Moreover, the crystal structure of $RETaO_4$ can also be influenced by processing conditions such as sintering temperature and cooling history. For example, $YTaO_4$ has been reported to crystallize into both *m* and *m*′ phases under different thermal treatment conditions [42]. In the present work, since each sample is synthesized under identical processing conditions, the average RE^{3+} ionic radius is considered to be the primary factor influencing the observed phase evolution. Therefore, selecting rare-earth elements with small ionic radii is important for promoting the formation of the *m*′ phase to achieve low TECs. Accordingly, Sc, Y, Tm, Ho, Dy, and Gd are selected as the principal components in this study. For RE^{3+} with a coordination number of 8, the ionic radii of these elements are close to this reference region, as shown in Table 1 [43]. The calculations show that the designed compositions have weighted-average RE^{3+} ionic radii lower than the reference region of approximately 0.100-0.102 nm, which favors the formation of *m*′-$RETaO_4$ HECs under the present synthesis conditions.

Therefore, a key question is whether non-equimolar compositional design can produce a more favorable local distortion state than conventional equimolar high-entropy design, thereby enabling the simultaneous optimization of TECs and thermal conductivity of *m*′-$RETaO_4$.

Table 1 Ionic radii (*r*/*nm*) of RE^{3+} ions with an oxygen coordination number of 8 [43].

Element	Sc^{3+}	Y^{3+}	Tm^{3+}	Ho^{3+}	Dy^{3+}	Gd^{3+}
r (nm)	0.0870	0.1019	0.0994	0.1015	0.1027	0.1053

Just Accepted

In this work, a series of non-equimolar *m*′-$RETaO_4$ HECs incorporating selected RE elements are designed and synthesized. The molar ratios are systematically varied to tune size mismatch and configurational entropy. In addition to standard characterization, physical descriptors, including lattice parameters (*a*, *b*, *c*), configuration entropy (S_{conf}), disorders in RE ionic radius (D_δ), atomic weight (D_w) and electronegativity (D_e), are introduced to clarify the underlying mechanisms. This study investigates the evolution of crystal structure, thermal expansion behavior, and thermal conductivity of non-equimolar $RETaO_4$ ceramics as EBCs.

2 Materials and methods

2.1 Synthesis of materials

The samples were fabricated via a conventional solid-state sintering route. First, RE_2O_3 (RE = Sc, Y, Tm, Ho, Dy, Gd) and Ta_2O_5 (purity ≥ 99.99 %, Macklin, China) were weighed according to the designed molar ratios and homogenized by ball milling at 300 $r \cdot min^{-1}$ for 12 h. The resulting slurry was dried at 70 °C for 24 h. The dried powders were sieved through a 300-mesh sieve and then pressed at 100 MPa for 3 min to obtain green compacts with a diameter of 15 mm and a thickness of 2 mm. The compacts were sintered at 1650 °C for 10 h. The six samples were denoted as $(Sc_{0.1}Y_{0.2}Tm_{0.2}Ho_{0.2}Dy_{0.2}Gd_{0.1})TaO_4$ (HE-1), $(Sc_{0.2}Y_{0.1}Tm_{0.2}Ho_{0.1}Dy_{0.2}Gd_{0.2})TaO_4$ (HE-2), $(Sc_{0.2}Y_{0.2}Tm_{0.2}Ho_{0.2}Dy_{0.1}Gd_{0.1})TaO_4$ (HE-3), $(Sc_{0.3}Y_{0.1}Tm_{0.1}Ho_{0.2}Dy_{0.1}Gd_{0.2})TaO_4$ (HE-4), $(Sc_{0.3}Y_{0.2}Tm_{0.1}Ho_{0.1}Dy_{0.1}Gd_{0.2})TaO_4$ (HE-5), and $(Sc_{0.4}Y_{0.1}Tm_{0.1}Ho_{0.1}Dy_{0.2}Gd_{0.1})TaO_4$ (HE-6).

2.2 Structural identifications

Phase structures were characterized by X-ray diffraction (XRD, Miniflex 600, Rigaku, Japan). XRD Rietveld refinement was performed using the General Structure Analysis System (GSAS-II) software. Grain morphology and elemental distribution were examined using a scanning electron microscope (SEM, JSM-7800F, JEOL, Japan) equipped with an energy-dispersive spectrometer (EDS, 6751A-6UUS-SN, Thermo Scientific, US). The HE-3 was prepared by the focused ion beam (FIB,

Just Accepted

FEI Scios 2, Gatan, USA) to conduct atomic characterizations within a transmission electron microscopy (TEM; Tecnai G2 F20, FEI, USA).

2.3 Measurements of thermal and mechanical properties

The samples used for thermal expansion measurements were cut into rectangular bars of 2 × 2 × 10 mm. The TECs were measured by dilatometer (DIL 402, Netzsch, Germany). For thermal diffusivity measurements, the samples were cut into disks with a diameter of 6 mm. The thermal diffusivity (α) was measured using a laser flash apparatus (LFA 457, Netzsch, Germany), and the detailed experimental parameters were described in previous studies [44, 45]. The thermal conductivity (k) was calculated using Eq. (1) based on the measured thermal diffusivity, density (ρ), porosity (φ), and heat capacity (C_p). The effect of porosity on thermal conductivity was corrected using Eq. (2) [46]. The actual density of each sample was measured by the Archimedes drainage method, and the relative porosity was calculated by comparing the bulk density with the theoretical density obtained from the XRD Rietveld refinement results. The relative densities of the synthesized ceramics were higher than 95%, which helped reduce the influence of pores on the accuracy of the thermal-property measurements. The C_p values used for calculating thermal conductivity were obtained from thermodynamic handbook [47].

$$k = \alpha \cdot \rho \cdot Cp \tag{1}$$

$$\frac{k}{k_0} = 1 - \frac{4}{3}\phi \tag{2}$$

Elastic properties were evaluated using an ultrasonic pulse-echo device (UMS-100, Teclab, France). The longitudinal (V_L) and transverse (V_T) sound velocities were measured to calculate the mean sound velocity (V_M), Poisson's ratio (ν), Young's modulus (E), Bulk modulus (B), Shear modulus (G) and Debye temperature (T_D) according to Eqs. (3-7) [19, 48]:

$$V_M = \left[\frac{1}{3}\left(\frac{1}{V_L^3} + \frac{2}{V_T^3}\right)\right]^{-\frac{1}{3}} \tag{3}$$

Just Accepted

$$\upsilon = \frac{1 - 2(V_{\mathrm{T}}/V_{\mathrm{L}})^2}{2 - 2(V_{\mathrm{T}}/V_{\mathrm{L}})^2} \tag{4}$$

$$E = \frac{\rho V_{\mathrm{T}}^2 (3V_{\mathrm{L}}^2 - 4V_{\mathrm{T}}^2)}{(V_{\mathrm{L}}^2 - V_T^2)} \tag{5}$$

$$B = \frac{E}{3(1 - 2\nu)} \tag{6}$$

$$G = \frac{E}{2(1 + \nu)} \tag{7}$$

3 Results and discussion

3.1 Configuration entropy and disorders of the designed HECs

To quantify the degree of structural complexity, the configurational entropy (S_{conf}), disorders in ionic size (D_δ), atomic weight (D_w), and electronegativity (D_e) of HE-1~HE-6 are first calculated using Eqs. (8-11) [49]:

$$\begin{aligned} \Delta S_{\mathrm{conf}} &= -R \sum_s m_s \sum_i x_{i,s} \ln x_{i,s} \\ &= -R \left[\left(\sum_{a=1}^{n} x_a \ln x_a \right)_{\mathrm{A-site}} + \left(\sum_{b=1}^{n} x_b \ln x_b \right)_{\mathrm{B-site}} + 4 \left(\sum_{c=1}^{n} x_c \ln x_c \right)_{\mathrm{C-site}} \right] \end{aligned} \tag{8}$$

$$D_\delta = \sqrt{\sum_{i=1}^{n} c_i \left(1 - \frac{\delta_i}{\bar{\delta}}\right)^2} \tag{9}$$

$$D_W = \sqrt{\sum_{i=1}^{n} c_i \left(1 - \frac{W_i}{\bar{W}}\right)^2} \tag{10}$$

$$D_e = \sqrt{\sum_{i=1}^{n} c_i \left(1 - \frac{e_i}{\bar{e}}\right)^2} \tag{11}$$

where m_s denotes the multiplicity of sublattice s, and $x_{i,s}$ denotes the fractional composition of element i within sublattice s; x_a, x_b, and x_c denote the molar fractions of ions at the A-, B-, and O-site, respectively. The c_i represents the molar fraction of the i-th component. The δ_i, W_i and e_i denote the

Just Accepted

ionic radius, atomic weight, and electronegativity of the *i*-th cation, respectively. The $\bar{\delta}$, $\bar{W}$ and $\bar{e}$ are the weighted average ionic radius, atomic weight, and electronegativity, respectively. The calculated physical parameters are summarized in Table 2.

Table 2 The configurational entropy (S_{conf}), disorders in ionic size (D_δ/%), atomic weight (D_w/%), and electronegativity (D_e/%) of the designed non-equimolar *m*′-$RETaO_4$ HECs

Sample	S_{conf}	D_δ	Dw	D_e
HE-1	1.7481*R*	4.79	33.00	3.44
HE-2	1.7481*R*	6.43	37.29	4.57
HE-3	1.7481*R*	6.17	38.27	4.43
HE-4	1.6957*R*	7.54	41.83	5.37
HE-5	1.6957*R*	7.55	42.28	5.39
HE-6	1.6094*R*	8.38	46.19	6.00

Table 2 shows that HE-1~HE-3 exhibit the high S_{conf} of 1.7481*R*, and HE-4~HE-5 exhibit the comparatively low S_{conf} of 1.6957*R*. Each ceramic has the configuration entropy higher than 1.51*R*, proving that they are HECs. HE-1 exhibits the lowest D_δ of 4.79 %, D_w of 33.00 %, and D_e of 3.44 %, whereas HE-6 shows the highest D_δ of 8.38 %, D_w of 46.19 %, and D_e of 6.00 %. Considering that six HECs have the same RE elements, their disorders are controlled by the fraction of different RE elements. The high configurational entropy is beneficial for increasing the structural stability, and further promotes the formation of single-phase ceramics. Therefore, the present non-equimolar design is not based only on the average RE^{3+} ionic radius. Instead, S_{conf}, D_δ, D_w, and D_e are used as compositional descriptors to evaluate the configurational complexity, ionic-size mismatch, atomic-mass fluctuation, and electronegativity disorder of the designed $RETaO_4$ HECs [50]. These descriptors provide the basis for discussing the effects of non-equimolar compositional design on crystal structure and thermophysical properties.

3.2 Crystal structures and detail lattice parameters

Just Accepted

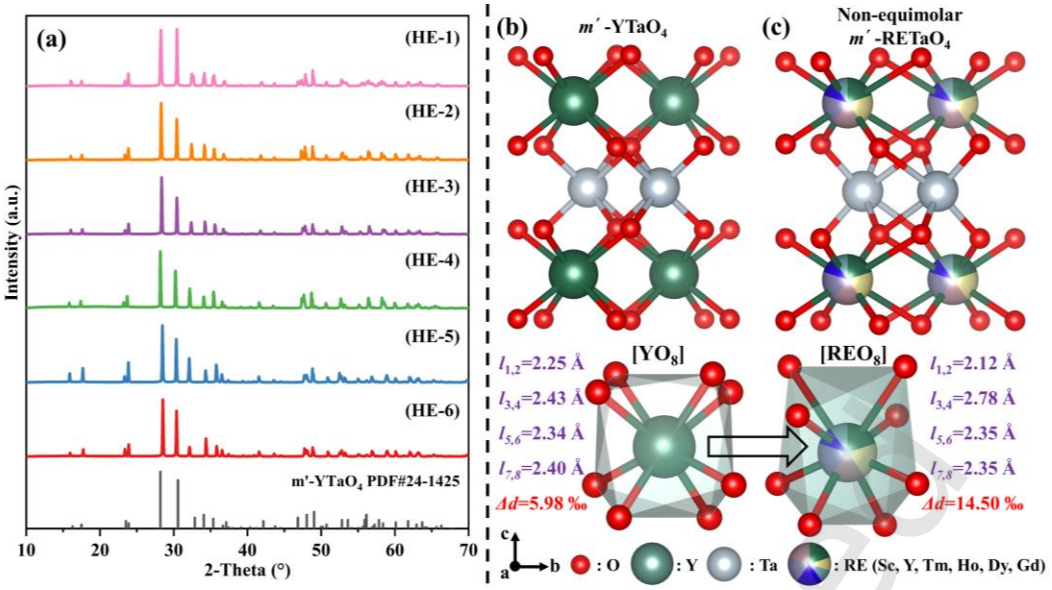

Fig. 1 Crystal structure characterizations of non-equimolar *m*´-$RETaO_4$ HECs, and their structures are compared with the *m*´-$YTaO_4$. (a) Comparisons of XRD patterns with the standard PDF card; (b) and (c) Comparisons of crystal structures between *m*´-$YTaO_4$ and *m*´-HECs.

Fig. 1(a) shows that the XRD patterns of the six non-equimolar $RETaO_4$ HECs are consistent with the standard card of *m*´-$YTaO_4$ (PDF#24-1425), indicating that they are crystallized into the *m*´ phase. The Ta-O coordination environments differ between the *m* and *m*´ phases of $RETaO_4$ ceramics. In the *m*´ phase, the crystal structure is mainly composed of distorted [REO_8] and [TaO_6] polyhedra, whereas the *m* phase contains [TaO_4] polyhedra. Therefore, the transition between the *m* and *m*´ phases is accompanied by a rearrangement of Ta-O coordination polyhedra and a change in the local structure [51, 52]. In the present work, the synthesized non-equimolar $RETaO_4$ HECs crystallize into the *m*´ phase, which is associated with their weighted average RE^{3+} ionic radii. Therefore, the subsequent structural analysis is focused on the distortion of [REO_8] and [TaO_6] polyhedra within the *m*´ phase. The XRD Rietveld refinement is conducted and shown in Fig. 2 to further confirm the detailed lattice parameters of each ceramic, which are listed in Table 3. Fig. 2 shows that the key indexes, i.e., *sig* and R_{wp} (%), of XRD Rietveld refinement are less than 2.00 and 9.00, respectively, indicating the high reliability of the refinement results. The good agreement between the experimental

Just Accepted

and calculated XRD patterns, together with the small difference curves, confirms that the *m*′-$YTaO_4$ structural model can reasonably describe the average crystal structures of the designed non-equimolar $RETaO_4$ HECs. The detailed lattice parameters prove that high-entropy effects and the high disorders in RE^{3+} ionic radius have greatly increased the distortion degree of polyhedra in the non-equimolar *m*′-$RETaO_4$ HECs.

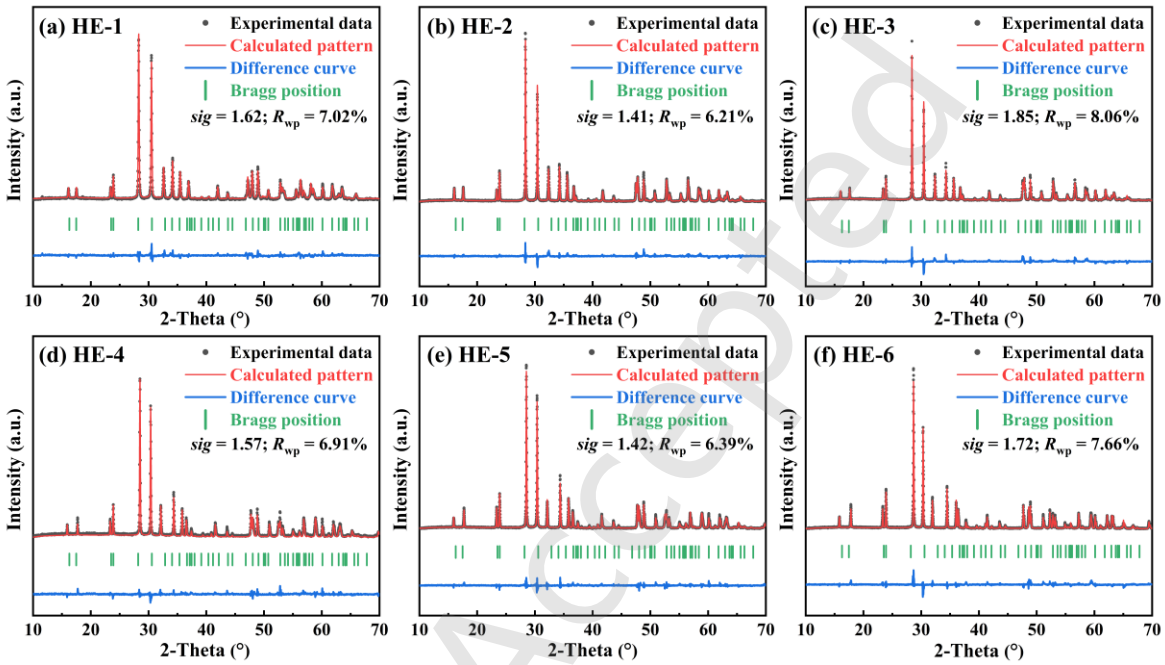

Fig. 2 XRD Rietveld refinement of non-equimolar *m*′-$RETaO_4$ HECs; (a)~(f) HE-1~HE-6, respectively.

Table 3 The lattice parameters (*a*, *b*, *c*/Å), beta angle (*β*/°), unit cell volume (V/Å^3), weighted average ionic radius ($\bar{r}_A$/nm), bulk density (ρ/g·cm^{-3}) and porosity (φ/%) of the non-equimolar *m*′-$RETaO_4$ HECs.

Sample	*a*	*b*	*c*	*β*	*V*	$\bar{r}_A$	*ρ*	*φ*
HE-1	5.26	5.53	5.07	95.64	146.763	0.1003	8.30	4.3
HE-2	5.24	5.57	5.04	95.03	146.495	0.0992	8.30	2.7
HE-3	5.28	5.49	5.09	96.05	146.428	0.0988	8.15	3.2
HE-4	5.24	5.57	5.03	95.06	146.391	0.0979	7.92	4.3

Just Accepted

HE-5	5.25	5.53	5.06	95.59	146.214	0.0979	7.87	2.9
HE-6	5.22	5.60	4.99	94.44	145.493	0.0962	7.85	2.7

Figs. 1(b) and (c) present the crystal structures and corresponding bond lengths in [REO_8] polyhedra of *m*′-$YTaO_4$ and the non-equimolar *m*′-$RETaO_4$ HECs, respectively. When the *A*-site is occupied by multiple RE^{3+} cations, the local coordination environment is altered, and the changes in distortion degree of [REO_8] and [TaO_6] polyhedra are calculated and compared, as summarized in Table 4. [19, 53].

$$\Delta d = \frac{1}{n}\sum_{n=1}^{N}\left[\frac{l_n - \bar{L}}{\bar{L}}\right]^2 \quad (12)$$

where l_n is the length of the *n*th chemical bond, and $\bar{L}$ is the average bond length of the polyhedron.

Compared with *m*′-$YTaO_4$, the non-equimolar *m*′-$RETaO_4$ HECs exhibit greater distortion degree (Δd) of polyhedral, and the Δd is increased from 5.98 ‰ of [YO_8] to 14.50 ‰ of [REO_8]. Notably, the highest distortion degree of [REO_8] polyhedral is observed in HE-3 (Δd=14.502 ‰), which is significantly higher than those of HE-1 (Δd=5.544 ‰) and HE-6 (Δd=12.920 ‰). This result indicates that the actual local structural distortion does not increase monotonically with S_{conf} or the theoretical disorder descriptors alone. Instead, the maximized distortion in HE-3 is more likely associated with a balanced interplay between configurational complexity and cationic mismatch, allowing the resulting local strain to be more fully accommodated within the crystal structure. Therefore, the experimentally observed high distortion degree of polyhedra in HE-1~HE-6 is not determined solely by any single compositional descriptor in current study.

The XRD Rietveld refinement provides average crystallographic information, including lattice parameters, average bond lengths, and average polyhedral distortion parameters. These refined structural parameters are used to compare the average structural evolution among the designed compositions, whereas the local structural disorder and lattice strain are further examined by TEM and GPA analyses in the following sections.

Just Accepted

Table 4 The bond lengths (l/Å), average bond length ($\bar{L}$/Å), distortion degree (Δd/‰) and polyhedral volume (Vp/Å^3) of [REO_8] and [TaO_6] polyhedra derived from the XRD Rietveld refinement.

Sample	Bond	Polyhedron	l				$\bar{L}$	Δd	Vp
m'-$YTaO_4$	Ta-O	[TaO_6]	1.850	1.959	2.228		2.015	5.975	9.879
	Y-O	[YO_8]	2.290	2.324	2.347	2.522	2.372	1.394	22.887
HE-1	Ta-O	[TaO_6]	1.934	2.054	2.260		2.083	4.178	10.695
	RE-O	[REO_8]	2.160	2.190	2.400	2.590	2.335	5.544	20.819
HE-2	Ta-O	[TaO_6]	1.822	2.065	2.114		2.000	4.074	10.081
	RE-O	[REO_8]	2.200	2.200	2.300	2.600	2.325	4.971	21.236
HE-3	Ta-O	[TaO_6]	1.961	2.020	2.341		2.108	6.270	11.924
	RE-O	[REO_8]	2.065	2.121	2.354	2.777	2.323	14.502	21.237
HE-4	Ta-O	[TaO_6]	1.873	2.017	2.075		1.989	1.824	9.441
	RE-O	[REO_8]	2.100	2.300	2.400	2.700	2.375	8.310	22.557
HE-5	Ta-O	[TaO_6]	1.895	2.201	2.331		2.142	7.278	8.974
	RE-O	[REO_8]	2.142	2.323	2.332	2.826	2.406	11.164	23.048
HE-6	Ta-O	[TaO_6]	1.799	1.806	2.105		1.903	5.615	8.630
	RE-O	[REO_8]	2.178	2.255	2.455	2.894	2.446	12.920	23.247

3.3 Microstructures and elemental distributions

Just Accepted

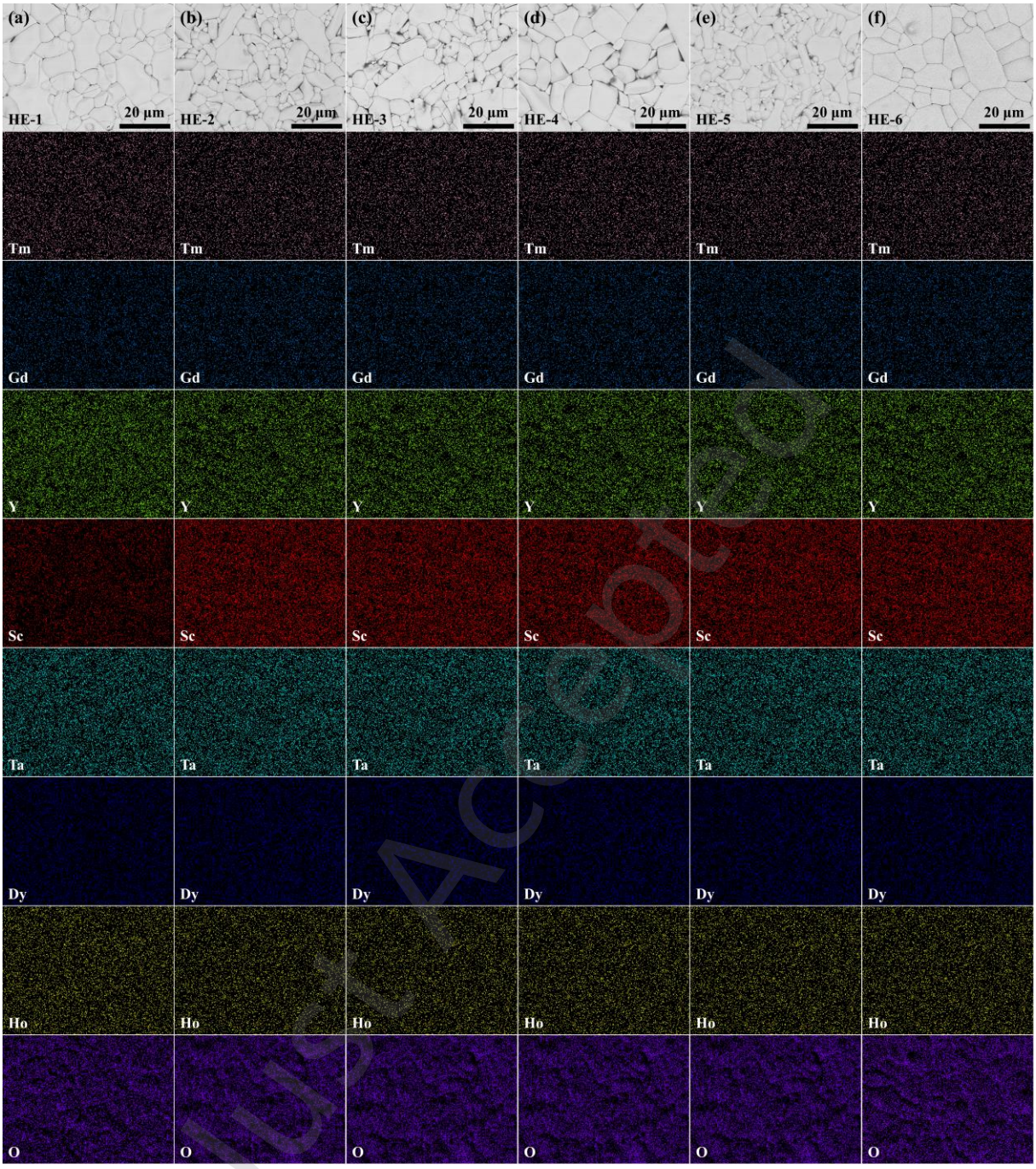

Fig. 2 Microstructures and EDS mappings of the non-equimolar *m*′-$RETaO_4$ HECs: (a-f) HE-1~HE-6, respectively.

Figs. 3(a)-(f) show the microstructures and corresponding EDS mappings of HE-1~HE-6, respectively. Each sample exhibits a dense microstructure with well-developed grains, without obvious secondary phases. The corresponding EDS mappings show uniform distributions of Sc, Y, Tm, Ho, Dy, Gd, Ta, and O within the observed regions, without obvious elemental segregation. These results

demonstrate the dense and compositionally homogeneous microstructures of the prepared non-equimolar $RETaO_4$ HECs.

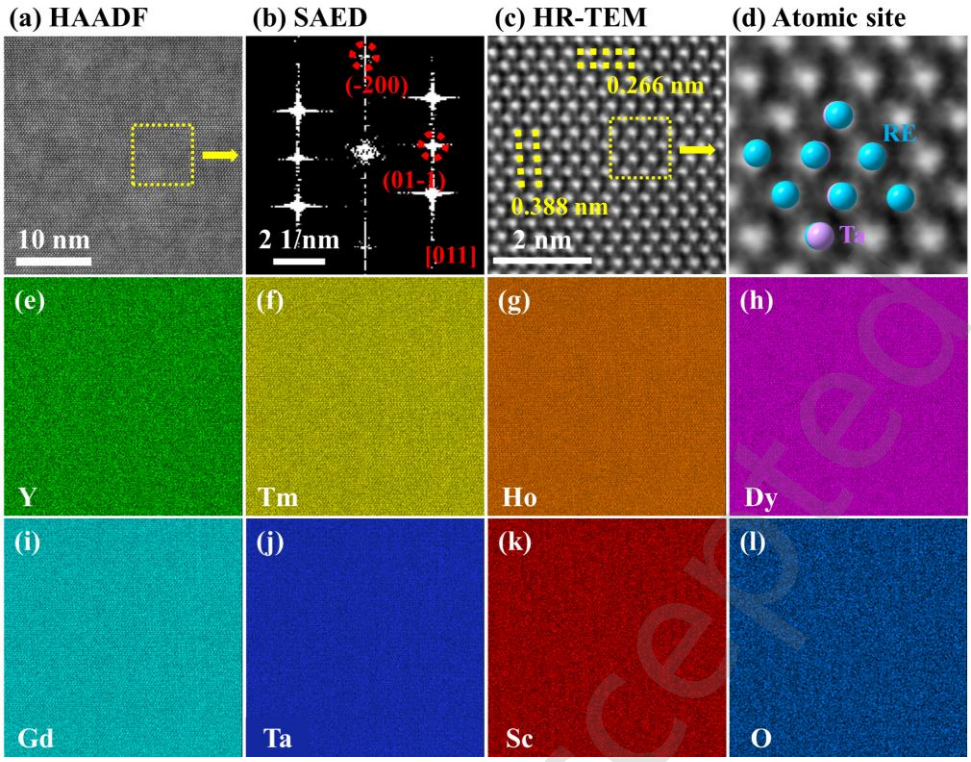

Fig. 3 Nanoscale microstructures and elemental distributions of HE-3: (a) HAADF; (b) FFT; (c) HR-TEM; (d) Atomic positions; (e)-(l) Nanoscale atomic distributions of each element.

Fig. 4 further reveals the nanoscale atomic positions and elemental distributions of HE-3, and the zone axis is confirmed as [011] as shown in Fig. 4(b). The interplanar spacing of (-200) and (01-1) is confirmed and marked as shown in Fig. 4(c), which are 0.266 and 0.388 nm, respectively. The aforementioned atomic structures are consistent with the lattice parameters obtained from the XRD Rietveld refinement. Fig. 4(d) shows the atomic position of RE and Ta atoms, and they occupy the same sites viewed from the [011] zone axis. Figs. 4(e)~(l) further reveal that each element is distributed uniformly at the nano scale, and no obvious segregation is found. The above situation indicates that the high polyhedral distortion degree is triggered by the high disorders in RE ionic radii and atomic weight, which may also lead to high lattice strains. It is well known that lattice strains can effectively

Just Accepted

scatter phonons to reduce thermal conductivity, and their effects will be further confirmed and discussed in the following parts [11, 54].

3.4 Elastic properties

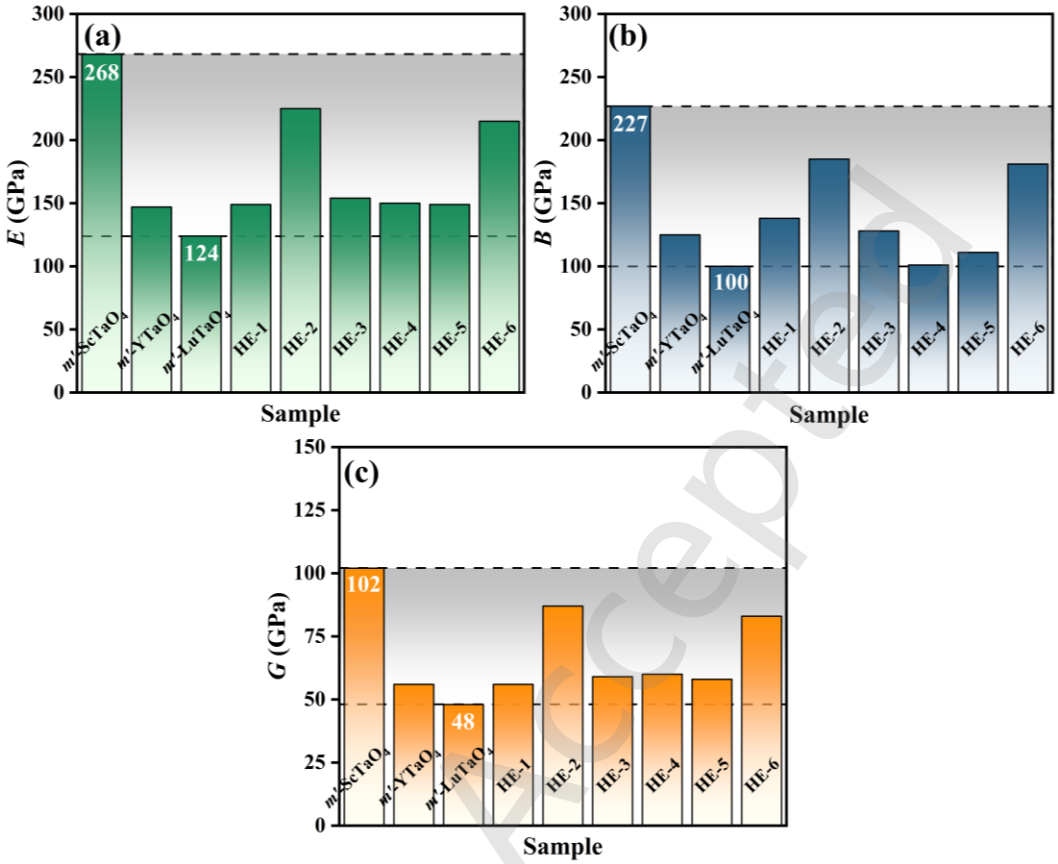

Fig. 4 Elastic properties of non-equimolar *m*′-$RETaO_4$ HECs compared with other *m*′-$RETaO_4$ [11, 19]: (a) Young′s modulus; (b) Bulk modulus; (c) Shear modulus.

Fig. 5 presents a comparative analysis of the elastic moduli between the non-equimolar $RETaO_4$ HECs and other *m*′-$RETaO_4$, including $ScTaO_4$, $YTaO_4$, and $LuTaO_4$ [11, 19]. *m*′-$ScTaO_4$ serves as the upper limit of the reference modulus range, while *m*′-$LuTaO_4$ serves as the lower limit. The prepared non-equimolar *m*′-$RETaO_4$ HECs have lower modulus than that of $ScTaO_4$, and have modulus higher than that of $LuTaO_4$. Among the synthesized samples, HE-2 and HE-6 exhibit relatively high elastic moduli.

Just Accepted

The elastic moduli provide information on the average bonding stiffness of the designed non-equimolar $RETaO_4$ HECs. In these compositions, multiple RE^{3+} cations with different ionic radii occupy the same A-site, which can change the average RE-O bond lengths and introduce heterogeneous local bonding environments around the [REO_8] polyhedra [19, 55]. Therefore, the elastic properties of the present HECs should not be simply interpreted by the content of a single cation, such as Sc^{3+}, but should be considered as the combined result of average RE^{3+} ionic radius, RE-O bond-length variation, polyhedral distortion, and local bonding heterogeneity. The reported equimolar $RETaO_4$ HECs exhibit Young's moduli ranging from 119.1 to 201.1 GPa [56]. The elastic moduli of the non-equimolar $RETaO_4$ HECs fall within this range but vary markedly among the six compositions, indicating that adjustment of the RE-site molar fractions enables composition-dependent regulation of elastic properties.

HE-2 and HE-6 exhibit relatively high elastic moduli among the synthesized compositions, which may be related to their relatively high contents of small-radius Sc^{3+} and the corresponding decrease in average RE-O bond length. However, the elastic moduli do not vary monotonically with Sc^{3+} content or the calculated disorder descriptors, indicating that non-equimolar compositional design affects elastic properties through coupled structural effects rather than a single compositional parameter. This trend is consistent with the XRD Rietveld refinement results, which show composition-dependent changes in [REO_8] and [TaO_6] polyhedral distortion. Therefore, the elastic modulus results further support that non-equimolar design modifies the average lattice stiffness and local bonding environment of *m*′-$RETaO_4$ HECs. The measured acoustic velocities and derived elastic parameters are subsequently used in the point-defect scattering analysis.

3.5 Thermal expansion performance

Just Accepted

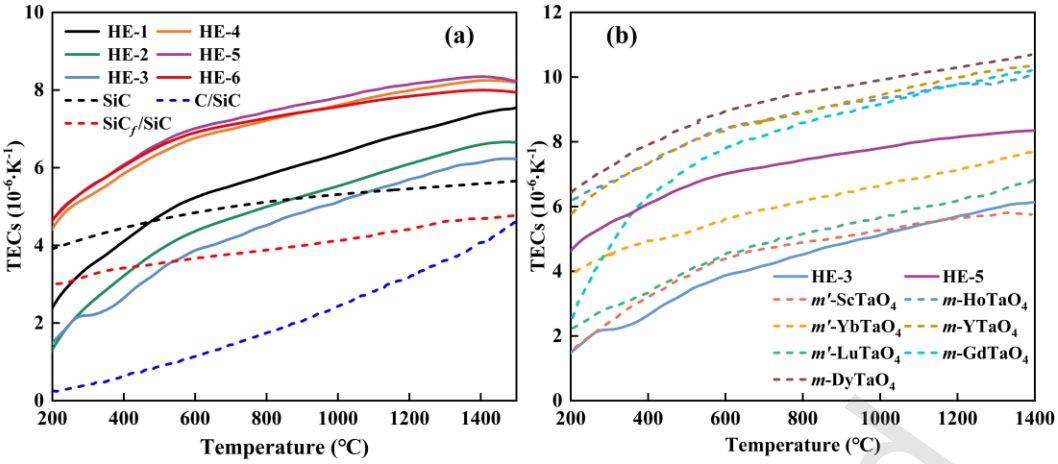

Fig. 5 Temperature-dependent TECs of non-equimolar *m*′-$RETaO_4$ HECs [15-19, 55, 57, 58]: (a) Comparison of TECs of HE-1~HE-6 with SiC, C/SiC, and SiC_f/SiC CMCs; (b) Comparison of TECs among HE-3, HE-5, and other $RETaO_4$ ceramics.

Fig. 6(a) compares the TECs of the HE-1~HE-6 at 200~1500 °C with those of SiC, C/SiC, and SiC_f/SiC composites [15-18, 58]. The TECs of HE-1~HE-6 increase monotonically with increasing temperature without abrupt changes, indicating that no phase transition occurs within the tested temperature, and confirming the excellent high-temperature phase stability. However, clear composition-dependent differences are observed among the six HECs. Among them, HE-3 exhibits the lowest TECs (1.3-6.2×10^{-6} K^{-1}, 200~1500 °C), whereas HE-4~HE-6 exhibit relatively high TECs (4.7-8.2×10^{-6} K^{-1}, 200~1500 °C), particularly at elevated temperatures. Compared with previously reported $RETaO_4$ HECs (approximately 6.2-10.48×10^{-6} K^{-1}, 100~1400 °C) and $RENbO_4$ HECs (approximately 8.3-10.8×10^{-6} K^{-1}, 200~1200 °C) [56, 59] , the TECs of HE-3 are lower and closer to those of SiC (3.9-5.6×10^{-6} K^{-1}, 200~1500 °C). Fig. 6(b) further compares the TECs of HE-3, HE-5, and other $RETaO_4$ ceramics [19, 55, 57]. HE-3 exhibits lower TECs at 200~1500 °C than other $RETaO_4$ ceramics, except $ScTaO_4$, demonstrating that HE-3 is a potential EBCs material for CMCs. Although HE-5 exhibits the highest TECs among the synthesized HECs, its TECs remains lower than those of *m*-$RETaO_4$ ceramics, which suggests that the non-equimolar high-entropy design effectively tailors thermal expansion behavior of $RETaO_4$.

Just Accepted

The synthesized non-equimolar $RETaO_4$ HECs crystallize into the same *m´* phase. Therefore, the composition-dependent TECs can be compared within the same *m´* structural framework without the influence of phase-dependent differences in Ta-O coordination [56, 60]. The reduced TECs of HE-3 are closely associated with the maximized polyhedral distortion parameter (Δd), indicating that the enhanced distortion of the $[REO_8]$ polyhedra is an important structural factor affecting macroscopic thermal expansion behavior. As revealed by the XRD Rietveld refinement results, the maximized $[REO_8]$ distortion of HE-3 is accompanied by pronounced variations in its refined RE-O bond lengths, reflecting changes in the average $[REO_8]$ coordination environment. These structural features may alter the response of the $[REO_8]$ framework to thermally activated atomic displacements and thereby contribute to the reduced TECs. The observed correlation between the $[REO_8]$ distortion parameters and TECs further supports that polyhedral distortion is an important structural factor contributing to the thermal expansion behavior of the present $RETaO_4$ HECs. Non-equimolar design of RE cations induces pronounced polyhedral distortion in *m´*-$RETaO_4$ HECs, which is primarily accommodated by the $[REO_8]$ polyhedra, whereas the $[TaO_6]$ polyhedra form a relatively rigid structural framework [19, 57].

Although HE-1 exhibits the high S_{conf}, and HE-6 exhibits the high disorder descriptors (D_δ, D_w, and D_e), HE-3 exhibits the most severe actual polyhedral distortion (Δd). Due to the interplay between S_{conf} and the theoretical disorder descriptors, HE-3 exhibits the most pronounced distortion degree of $[REO_8]$ polyhedra, which is associated with enhanced local structural flexibility at the atomic scale [61-63]. This result indicates that the TECs of the present non-equimolar $RETaO_4$ HECs are not controlled only by the average RE^{3+} ionic radius. Different from $RETaO_4$ ceramics, the designed HECs contain the same set of RE cations, and their structural evolution is mainly regulated by the varied molar fractions of these cations. Therefore, the composition-dependent TECs are more closely associated with the actual $[REO_8]$ polyhedral distortion and local structural accommodation than with the average RE^{3+} ionic radius alone.

Just Accepted

With increasing temperature, atomic thermal vibrations become more pronounced, and the TECs increase accordingly. A plausible explanation is that the strongly distorted local coordination environment in HE-3 provides greater structural flexibility, which partially accommodates thermally activated atomic displacements and thereby suppressing macroscopic thermal expansion behavior. When the aforementioned local accommodation becomes insufficient, the thermal activation will translate into lattice expansion, and lead to an increment in TECs [64, 65]. Herein, the high distortion degree of [REO_8] in the non-equimolar *m*′-$RETaO_4$ HECs is considered to contribute to the reduced TECs by affecting local structure and lattice distortion. Therefore, tailoring polyhedral distortion through non-equimolar compositional design provides a feasible strategy for regulating the TECs of complex oxides.

3.6 thermal conductivity performance

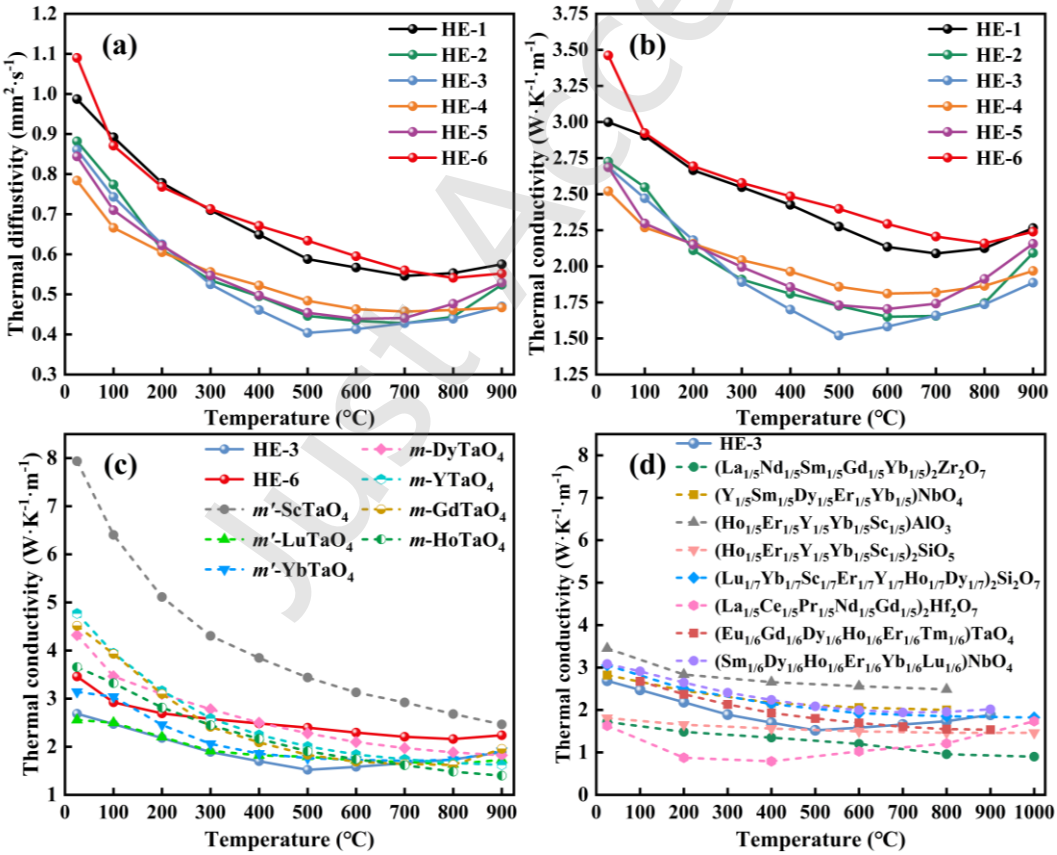

Fig. 6 Thermal transport properties of non-equimolar $RETaO_4$ HECs [19, 55-57, 59, 66, 67]. (a) Thermal diffusivities at 25~900 °C; (b) Thermal conductivities at 25~900 °C; (c) Comparisons of

Just Accepted

thermal conductivities among HE-3, HE-6, and other $RETaO_4$ ceramics; (d) Comparisons of thermal conductivities between HE-3 and other HECs.

Figs. 7(a)-(b) show the thermal diffusivities and conductivities decrease with increasing temperature from 25 to 700 °C, while they increase slightly from 700 to 900 °C. The decrease in *k* at 25-700 °C is mainly governed by the anharmonicity of lattice vibrations, i.e., the Umklapp phonon scattering processes [59, 68-70]. With increasing temperature, the phonon mean free path is significantly reduced, leading to a decrease in *k*. The slight increase in thermal conductivity at 700-900 °C is attributed to radiative heat transfer, which partially compensates for the reduction in *k* caused by phonon scattering. Among the studied HECs, HE-3 exhibits the lowest *k* of 1.52-2.68 $W \cdot m^{-1} \cdot K^{-1}$, while HE-6 exhibits the highest *k* of 2.16-3.46 $W \cdot m^{-1} \cdot K^{-1}$ at 25~900 °C. Fig. 7(c) compares the *k* of HE-3 and HE-6 with those of other $RETaO_4$ ceramics [19, 55, 57]. Because no *m*-*m´* phase transition or mixed Ta-O coordination framework is observed in the present HECs, the differences in thermal conductivity are associated with the combined effects of local lattice strain, polyhedral distortion, RE-site disorder, and RE-O bonding heterogeneity within the *m´* phase. HE-3 exhibits a markedly lower *k* than most $RETaO_4$ ceramics. Although HE-6 shows the highest *k* among the studied HECs, its thermal conductivity is still lower than many other $RETaO_4$ ceramics, proving the excellent thermal insulation performance of non-equimolar $RETaO_4$ HECs. Fig. 7(d) compares the *k* of HE-3 with those of other HECs as EBCs candidate [56, 59, 71-74]. Overall, HE-3 exhibits lower *k* than most of the compared $RETaO_4$ HECs, $RENbO_4$ HECs, and other HECs. Although some high-entropy zirconates and hafnates exhibit lower *k*, HE-3 still shows competitive thermal insulation performance among these oxides. Accordingly, it can be seen that the non-equimolar high-entropy design can effectively reduce thermal conductivity of $RETaO_4$, which is associated with the coupled effects of RE-site disorder, polyhedral distortion, and local lattice strain. Herein, the origins of low thermal conductivity of these non-equimolar $RETaO_4$ HECs may be related to the local structural heterogeneity introduced by the non-equimolar compositional design.

Just Accepted

3.7 Origins of the low thermal conductivity

For the designed non-equimolar $RETaO_4$ HECs, the high disorders in RE atomic weight and ionic radius can enhance the phonon scattering to reduce thermal conductivity, and we compare the experimentally measured thermal conductivity (k_{exp}) with the theoretically predicted thermal conductivity (k_{cal}) derived from the phonon point defect scattering theory. The theoretically predicted thermal conductivity is calculated using Eqs. (13-18) [75, 76]. At temperatures above the Debye temperature, the ratio of the lattice thermal conductivities of a material containing defects to that of the parent material without defects can be written as

$$\frac{k_{\text{cal}}}{k} = \frac{\tan^{-1}(u)}{u} \tag{13}$$

here k_{cal} and k are the thermal conductivities of the defect-containing material and the parent material, respectively. In the present calculation, m'-$YbTaO_4$ is taken as the parent material for HE-1, HE-3, HE-4, and HE-5, while m'-$ScTaO_4$ is taken as the parent material for HE-2 and HE-6. The parameter u is defined by

$$u = \left(\frac{\pi^2 T_D \overline{V}}{h v^2} k\Gamma_{Total}\right)^{1/2} \tag{14}$$

where h, v, T_D, $\overline{V}$ stand for the Planck constant, mean sound velocity, Debye temperature and the average volume per atom. The parameter T_D is defined by

$$T_D = \frac{h}{k_B}\left(\frac{3m}{4\pi V}\right)^{1/3} V_M \tag{15}$$

where k_B, m, V represented the Boltzmann constant, atomic mass and atomic volume, respectively. The imperfection scaling parameter Γ_{Total}, representing the strength of point defects phonon scattering, always has two components, the scattering parameter due to mass fluctuations Γ_M, and the scattering parameter due to strain-field fluctuations Γ_S. The point-defect scattering model primarily considers mass and strain-field fluctuations as the dominant scattering sources. The contribution of electronegativity disorder to phonon scattering has not yet been incorporated into a generally accepted

Just Accepted

quantitative model, particularly for rare-earth multicomponent systems. Therefore, the present analysis focuses on the effects of mass and strain-field fluctuations on phonon scattering behavior.

$$\Gamma_{\text{Total}} = \Gamma_{\text{M}} + \Gamma_{\text{S}} = \sum c_i \left(\frac{M_i - \bar{M}}{\bar{M}}\right)^2 + \varepsilon \sum c_i \left(\frac{r_i - \bar{r}}{\bar{r}}\right)^2 \quad (16)$$

where $\bar{M}$ represents the average mass of (Sc, Y, Tm, Ho, Dy, Gd), M_i represents the mass of the corresponding atom, c_i represents the fractional concentration of the corresponding atom, and ε is the phenomenological fitting parameter governing the strain-field scattering strength.

$$\varepsilon = \frac{2}{9}\left(6.4\frac{1+\nu}{1-\nu}\gamma\right)^2 \quad (17)$$

where γ is the Grüneisen parameter calculated using Eq. (18).

$$\gamma = \frac{3(1+\nu)}{2-3\nu} \quad (18)$$

In the present point-defect scattering model calculation of thermal conductivity, *m*′-$YbTaO_4$ is used as the reference parent material for HE-1, HE-3, HE-4, and HE-5, while *m*′-$ScTaO_4$ is used as the reference parent material for HE-2 and HE-6. This selection is made based on the structural and physical similarities between the parent materials and the corresponding $RETaO_4$ HECs [19, 77, 78]. For HE-1, HE-3, HE-4, and HE-5, *m*′-$YbTaO_4$ has the same *m*′-$RETaO_4$ crystal structure as the prepared HECs, and its Yb^{3+} ionic radius, acoustic velocity, and relevant elastic parameters are comparable to those of these $RETaO_4$ HECs. For HE-2 and HE-6, *m*′-$ScTaO_4$ is selected because these two compositions exhibit relatively high elastic moduli, and HE-6 contains the highest Sc fraction and is compositionally close to $ScTaO_4$. These structural and physical similarities are relevant to the point-defect scattering model because the mean sound velocity, Debye temperature, average atomic volume, mass and radius fluctuation terms, Poisson's ratio, and Grüneisen parameter are involved in Eqs. (13-18). Therefore, these two reference parent materials provide a more appropriate benchmark for evaluating phonon scattering effects related to misfits in ionic radius and atomic weight. Accordingly,

Just Accepted

the calculated thermal conductivities are used for comparisons with the experimental values as shown in Fig. 8.

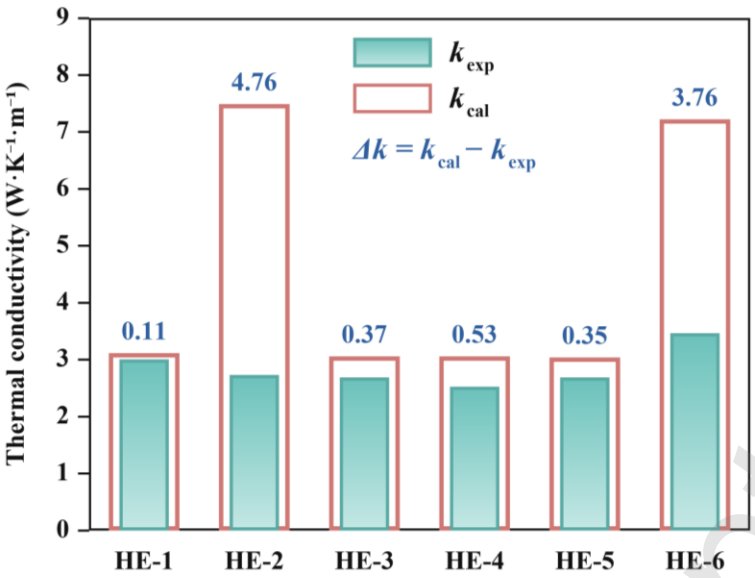

Fig. 7 Comparisons between k_{exp} and k_{cal} at 25 ºC of non-equimolar $RETaO_4$ HECs.

Fig. 8 shows that the k_{exp} is lower than k_{cal} of HE-1~HE-6. The point-defect scattering model mainly considers the average parameters related to point defects, whereas the additional reduction in k for HE-1~HE-6 is closely associated with local structural factors that are not fully described by the average point defect model, including the severe distortion degree of polyhedron, high lattice strain, RE-O bond-length disorder, and bonding-strength heterogeneity [79, 80]. Therefore, the comparison between k_{exp} and k_{cal} can serve as a reference for evaluating additional phonon scattering effects. The grains of the prepared ceramics are micrometer scale, which is much larger than the nanometer scale of phonon mean free path. Therefore, grain boundary scattering on phonons is omitted. In addition, the effect of porosity on thermal conductivity is corrected using Eq. (2) before the experimental and calculated values are compared. The SEM observations also show the dense microstructures without observable pores or microcracks for HE-1~HE-6. Therefore, grain boundaries, porosity, and microcracks are not considered as the primary origins of the discrepancy between k_{exp} and k_{cal}.

The RE-O bond-length disorder originates from the occupation of the same A-site by multiple RE^{3+} cations with distinct ionic radii. In the present non-equimolar $RETaO_4$ HECs, the ionic radius of

Just Accepted

RE^{3+} varies from 0.0870 nm for Sc^{3+} to 0.1053 nm for Gd^{3+}, which can produce heterogeneous local coordination environments around the [REO_8] polyhedra. The XRD Rietveld refinement results show that the RE-O bond lengths within the [REO_8] polyhedra are broadly distributed. For example, the RE-O bond lengths in HE-3 range from 2.065 to 2.777 Å, indicating pronounced bond-length disorder within the local coordination structure. Such bond-length disorder can generate local strain fields and enhance phonon scattering, which is consistent with the strain-field scattering contribution considered in the point-defect scattering model.

In addition to the strain-field effect, the variation in RE-O bond lengths may also imply possible RE-O bonding heterogeneity. Such local bonding heterogeneity can create spatially different vibrational environments, which may disturb phonon propagation and further shorten the phonon mean free path. Therefore, local lattice distortion, strain fluctuation, RE-O bond-length disorder, polyhedral distortion, and possible RE-O bonding heterogeneity are considered as important structural factors contributing to enhanced phonon scattering in the present non-equimolar $RETaO_4$ HECs [59, 64, 81].

Figs. 9(a)-(c) show the local lattice strain distribution in HE-3 visualized by geometric phase analysis (GPA). The GPA results of the representative HE-3 sample provide local structural evidence of high lattice strains, while the structural descriptors and thermophysical properties of HE-1~HE-6 suggest that local distortion and strain-related effects are important across the non-equimolar series. In the present work, GPA is used as a qualitative method to reveal local strain fluctuations at the atomic scale, rather than to directly quantify the reduction in thermal conductivity or phonon scattering coefficients. The strain contrast in the GPA maps indicates the presence of pronounced local lattice distortion in HE-3. In addition, the atomic intensity profiles along lines 1-4 in Fig. 9(d) and (f), exhibit obvious fluctuations, suggesting heterogeneous atomic arrangements at different positions. These observations provide structural evidence that RE-site disorder and polyhedral distortion induce local lattice strain fluctuations. Based on the elastic modulus and Debye temperatures of different $RETaO_4$ ceramics and HECs [19, 57], different RE-O bonding environments are expected to exhibit different

Just Accepted

bonding strengths. In particular, the large difference in ionic radius among RE^{3+} cations can introduce spatial variations in RE-O bond lengths and local bonding stiffness. Such bonding heterogeneity may enhance local lattice distortion and strain fluctuation, thereby contributing to stronger phonon scattering [56]. Fig. 9(f) shows the [REO_8], [TaO_6], and [TaO_4] polyhedra in *m*′-$YTaO_4$, *m*′-$ScTaO_4$, and *m*-$DyTaO_4$, which are reported in our previous studies [11, 19, 55]. The distortion degree of various polyhedra is different, thereby enhancing the lattice strains and leading to a low thermal conductivity in current studies. Accordingly, the reduced thermal conductivity of the studied non-equimolar $RETaO_4$ HECs is closely associated with enhanced phonon scattering induced by RE-site disorder, polyhedral distortion, RE-O bond-length fluctuations, bonding-strength variations, and the resulting local lattice strains. The GPA results provide structural visualization of these local strain characteristics, supporting the interpretation that lattice strain contributes to phonon scattering. However, GPA cannot quantitatively determine the phonon scattering coefficient or the exact contribution of lattice strain to thermal conductivity. Quantitative evaluation of these effects would require further theoretical calculations or dedicated phonon transport models [70, 81]. The deviation between the experimental and calculated thermal conductivities indicates that the point-defect scattering model does not fully capture the combined effects of local lattice strain, polyhedral distortion, RE-O bond-length fluctuations, possible bonding-strength heterogeneity, and model simplifications. Therefore, lattice strain is regarded as one important factor for reducing thermal conductivity of $RETaO_4$ HECs in this work.

Just Accepted

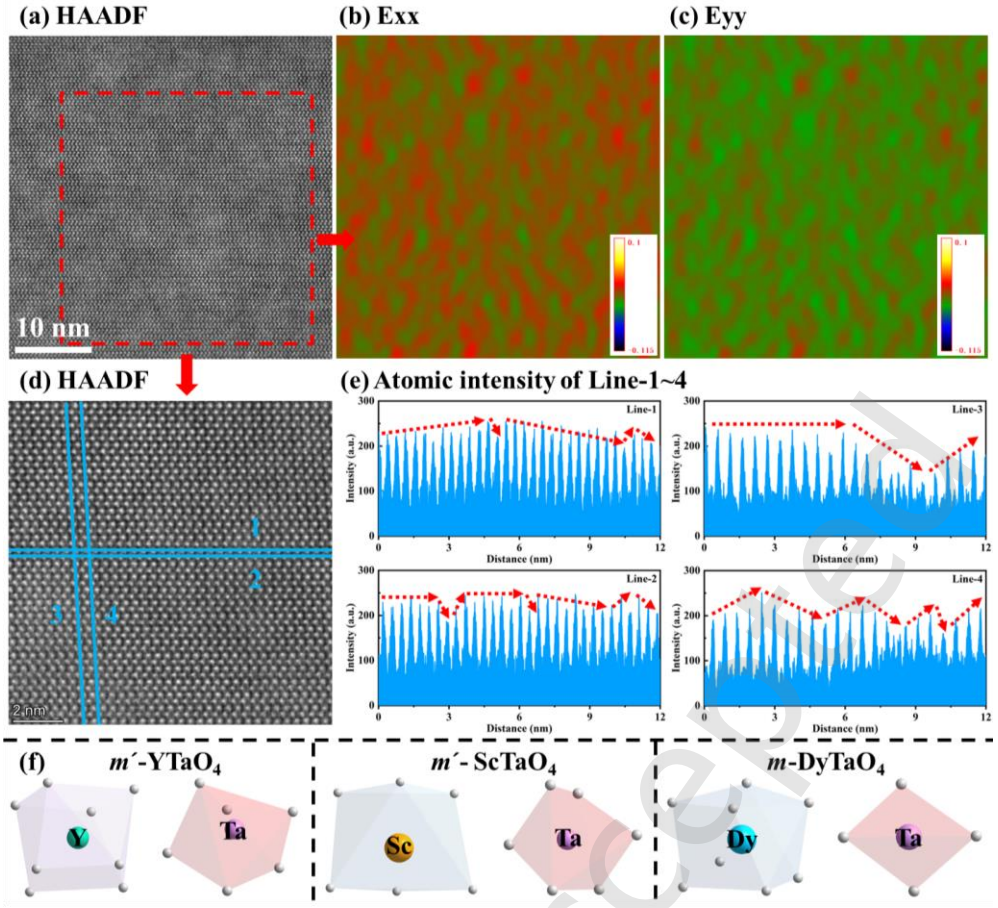

Fig. 9 The atomic structures and their atomic intensity along different directions in HE-3. (a)-(c) Atomic structures and the related GPA images used to identify the lattice strains; (d)-(e) The enlarged HAADF and corresponding atomic intensity; (f) The obvious differences in RE-O bond lengths and strengths, and the distortion degree of [REO_8] and [REO_6] polyhedra of different $RETaO_4$ ceramics.

4 Conclusions

This study investigates the composition-structure-property relationships in non-equimolar *m´*-$RETaO_4$ HECs, and elucidates the key structural factors associated with thermal expansion behavior and thermal conductivity. The designed and synthesized non-equimolar $RETaO_4$ HECs are crystallized into the *m´* phase due to the weighted-average RE^{3+} ionic radii er than the reference region of approximately 0.100-0.102 nm. The non-equimolar design can boost the distortion degree of polyhedra and lattice complexity, which increases the lattice strains as indicated by GPA images. The high distortion degree of [REO_8] polyhedra is closely associated with reduced TECs by affecting local

Just Accepted

structural flexibility and thermally activated lattice response. Among the designed compositions, HE-3, i.e., $(Sc_{0.2}Y_{0.2}Tm_{0.2}Ho_{0.2}Dy_{0.1}Gd_{0.1})TaO_4$, is considered as EBCs candidate for SiC-based CMCs owing to its relatively low TECs of 6.2×10^{-6} K^{-1} at 1500 °C, while the other compositions demonstrate the effectiveness of non-equimolar design in tailoring the thermal expansion behavior of $RETaO_4$ ceramics. The traditional point-defect scattering theory cannot effectively predict the thermal conductivity of the non-equimolar $RETaO_4$ HECs because it only considers the effects of disorders in RE^{3+} ionic radius and atomic weights, while additional phonon scattering associated with local lattice strains, polyhedral distortion, RE-O bond-length fluctuation, and possible bonding-strength heterogeneity is not included. The non-equimolar design strategy can effectively reduce thermal conductivity (1.52-2.68 $W\cdot m^{-1}\cdot K^{-1}$ at 25~900 °C) of $RETaO_4$ HECs, and the effects of high lattice strains should be considered in various HECs. This work proposes that polyhedral distortion, local lattice strains, and RE-O bonding heterogeneity are important structural factors for regulating the TECs and thermal conductivity of $RETaO_4$ HECs, and more works can be done to tailor thermal properties of various ceramics.

Availability of data and materials

The data that support the findings of this study are available from the corresponding author upon reasonable request.

Competing interests

The authors declare that they have no known competing financial interests or personal relationship that could have appeared to influence the work reported in this paper.

Author contributions

Bingyan Wu: investigation, methodology, formal analysis, data curation, visualization, original draft writing. Guangrong Li: methodology, visualization, writing-reviewing and editing, funding acquisition, and supervision. Lin Chen: methodology, visualization, writing-reviewing and editing, funding acquisition, and supervision. Jiankun Wang: methodology, visualization, analysis. Wei Pan:

Just Accepted

methodology, visualization, analysis. Jing Feng: conceptualization, funding acquisition, supervision, project administration, writing-reviewing and editing.

Acknowledgements

This work is supported by the National Natural Science Foundation (No. 52502065 and 52562006), and State Key Laboratory for Mechanical Behavior of Materials (No. 20252705).

References

[1] George K, Konstantinos S. Ceramic matrix composites for aero engine applications—A review. *Appl Sci* 2023, **13**: 3017.

[2] Oriol GD, Gonzalo GL, Liao ZR*, et al.* The new challenges of machining ceramic matrix composites (CMCs): review of surface integrity. *Int J Mach Tools Manuf* 2019, **139**: 24–36.

[3] Tang WB, Dong SJ, Zhou CL*, et al.* Thermal insulation performance of $PrAlO_3$ thermal barrier coating based on flame ablation measurement. *J Chin Soc Rare Earths* 2026, **44**: 209–218.

[4] Ward TZ, Wilkerson RP, Musicó BL*, et al.* High entropy ceramics for applications in extreme environments. *J Phys Mater* 2024, **7**: 021001.

[5] Nair RB, Brabazon D. Calcia magnesia alumino silicate (CMAS) corrosion attack on thermally sprayed thermal barrier coatings: a comprehensive review. *npj Mater Degrad* 2024, **8**: 44.

[6] Deng LW, Wang Y, Zhang XD. Enhancing the anti-CMAS corrosion performance of EBCs via adding SiC to $Yb_2Si_2O_7$ top ceramic layer: A novel SiC-$Yb_2Si_2O_7$/Si EBCs strategy. *J Eur Ceram Soc* 2026, **46**: 117847.

[7] Zan YX, Huang L, Gu WZ*, et al.* A nacre formation-inspired dynamic self-generating barrier for environmental deposit-resistant thermal barrier coatings. *J Adv Ceram* 2026, **15**: 9221218.

[8] Luo JC, Li C, Zhang HX*, et al.* Oxidation behavior of YGdSi silicide at 1500°C. *Corros Commun* 2026, https://doi.org/10.1016/j.corcom.2026.03.002.

[9] Wei P, Liu YW, Bai H*, et al.* A universal laser-driven controllable synthesis methodology enabling electromagnetic absorption in high-entropy rare-earth oxides. *Adv Mater* 2026, **38**: e20122.

Just Accepted

[10] Gan MD, Chong XY, Lu TL*, et al.* Unveiling thermal stresses in $RETaO_4$ (RE = Nd, Sm, Eu, Gd, Tb, Dy, Ho and Er) by first-principles calculations and finite element simulations. *Acta Mater* 2024, **271**: 119904.

[11] Chen L, Hu MY, Zheng XD*, et al.* Characteristics of ferroelastic domains and thermal transport limits in HfO_2 alloying $YTaO_4$ ceramics. *Acta Mater* 2023, **251**: 118870.

[12] Luo ZW, Dong SJ, Zhou CL*, et al.* Thermal cycling and water vapor corrosion resistance of $(Sc_{0.2}Ho_{0.2}Er_{0.2}Yb_{0.2}Lu_{0.2})_2Si_2O_7$ TEBCs. *J Chin Soc Rare Earths* 2025, **43**: 751–760.

[13] Yan K, Yu HY, Xiang Y*, et al.* Failure mechanism of Yb_2O_3-Gd_2O_3-Y_2O_3 co-doped zirconia double ceramic thermal barrier coating in Na_2SO_4+V_2O_5 environment. *Corros Prot* 2024, **45**: 23–29.

[14] Wang JK, Chen L, Zhang LY*, et al.* Structural evolutions and failure mechanisms of APS tantalate high-entropy ceramics coatings response to thermal cycle up to 1500 ºC. *J Adv Ceram* 2026, **15**: 9221261.

[15] Shen XL, Zhang S, Liu X*, et al.* Prediction of the thermo-mechanical properties of the SiC_f/SiC RVE model via FEM and asymptotic homogenization method: process and implementation details. *Arch Comput Methods Eng* 2021, **28**: 3067–3085.

[16] Lee KN. Current status of environmental barrier coatings for Si-Based ceramics. *Surf Coat Technol* 2000, **133-134**: 1–7.

[17] Spitsberg I, Steibel J. Thermal and environmental barrier coatings for SiC/SiC CMCs in aircraft engine applications. *Int J Appl Ceram Technol* 2004, **1**: 291–301.

[18] Zheng RY, Yang CP, Jia F. Evolution model of thermal expansion coefficient for 2D-C/SiC composites. *Acta Mater Compos Sin* 2024, **41**: 2083–2098.

[19] Chen L, Hu MY, Guo J*, et al.* Mechanical and thermal properties of $RETaO_4$ (RE = Yb, Lu, Sc) ceramics with monoclinic-prime phase. *J Mater Sci Technol* 2020, **52**: 20–28.

Just Accepted

[20] Gan MD, Chong XY, Yu W*, et al.* Understanding the ultralow lattice thermal conductivity of monoclinic $RETaO_4$ from acoustic-optical phonon anti-crossing property and a comparison with ZrO_2. *J Am Ceram Soc* 2023, **106**: 3103–3115.

[21] Chen L, Hu MY, Feng J. Mechanical properties, thermal expansion performance and intrinsic lattice thermal conductivity of $AlMO_4$ (M=Ta, Nb) ceramics for high-temperature applications. *Ceram Int* 2019, **45**: 6616–6623.

[22] Wang LY, Wang SQ, Chen GL*, et al.* Ceramic-based abradable sealing coatings for advanced aeroengines: Materials design, structural strategies, and multifunctional performance. *Extreme Mater* 2025, **1**: 33–58.

[23] Wei P, Bai H, Liu Y*, et al.* Composition engineering of high-entropy rare-earth monosilicates enables remarkable CMAS corrosion resistance. *J Materiomics* 2025, **11**: 100967.

[24] Wang YL, Zhang J, Wu TB*, et al.* Full-scale insight into high-entropy ceramics from basic concepts, synthesis technologies, structural characteristics, and properties to application prospects. *J Mater Res Technol* 2024, **33**: 398–430.

[25] Zhang JL, Liang JL, Li H*, et al.* A review of high-entropy ceramics preparation methods, properties in different application fields and their regulation methods. *J Mater Res Technol* 2024, **32**: 1083–1117.

[26] Hu HY, Zhang X, Huang TY*, et al.* Unraveling high-temperature corrosion mechanisms of eutectic high-entropy alloys in molten $MgCl_2$-NaCl-KCl. *Corros Commun* 2026, https://doi.org/10.1016/j.corcom.2026.03.010.

[27] Xue GY, Chen L, Feng J. Thermal properties of fluorite $Y_{3-x}(Ca_{x/4}In_{x/4}Mg_{x/4}Al_{x/4})NbO_7$(x=0.1, 0.2) high entropy ceramics. *J Chin Soc Rare Earths* 2026, **44**: 14–24.

[28] Liu HL, Pang S, Liu CQ*, et al.* High-entropy yttrium pyrochlore ceramics with glass-like thermal conductivity for thermal barrier coating application. *J Am Ceram Soc* 2022, **105**: 6437–6448.

Just Accepted

[29] Tadeusz M, Florianne V, Daniel J*, et al.* High-temperature transport properties of entropy-stabilized pyrochlores. *J Appl Phys* 2024, **135**: 085112.

[30] Rost CM, Schmuckler DL, Bumgardner C*, et al.* On the thermal and mechanical properties of $Mg_{0.2}Co_{0.2}Ni_{0.2}Cu_{0.2}Zn_{0.2}O$ across the high-entropy to entropy-stabilized transition. *APL Mater* 2022, **10**: 121108.

[31] Li R, He L, Lin N*, et al.* Synthesis, mechanical properties and thermal conductivity of high-entropy $(TiTaNbZrMo_x)(CN)$ ceramics. *J Eur Ceram Soc* 2023, **43**: 7273–7281.

[32] Chen ZY, Wang YZ, Huang YL*, et al.* Investigation on improving the comprehensive performance of environmental barrier coating materials by high-entropy multiphase design. *npj Mater Degrad* 2024, **8**: 37.

[33] Liu SX, Du MR, Ge YF*, et al.* Enhancement of high entropy oxide $(La_{0.2}Nd_{0.2}Sm_{0.2}Gd_{0.2}Y_{0.2})_2Zr_2O_7$ mechanical and photocatalytic properties via Eu doping. *J Mater Sci* 2022, **57**: 7863–7876.

[34] Luo ZW, Jiang JN, Dong SJ*, et al.* $(Gd_{0.2}Ho_{0.2}Er_{0.2}Yb_{0.2}Lu_{0.2})_2Si_2O_7$ and $(Sc_{0.2}Ho_{0.2}Er_{0.2}Yb_{0.2}Lu_{0.2})_2Si_2O_7$ high-entropy rare-earth disilicates as promising materials for environmental barrier coatings. *Ceram Int* 2024, **50**: 23342–23355.

[35] Li YR, Pan DH, Cao JH*, et al.* Recent advances in high-entropy ceramics: Design principles, structural characteristics, and emerging properties. *Extreme Mater* 2025, **1**: 42–72.

[36] Xue GY, Wang JK, Li CY*, et al.* High-entropy effects enhance atomic displacements to manipulate thermal/oxygen ionic transport properties of ordered RE_3MO_7 ceramics. *Rare Met* 2025, **44**: 10660–10671.

[37] Chen ZY, Huang YL, Peng F*, et al.* Non-equimolar multi-principal element monosilicates with excellent corrosion resistance. *J Am Ceram Soc* 2025, **108**: e20265.

[38] Liu YC, Jia DC, Zhou Y*, et al.* $Zn_{0.1}Ca_{0.1}Sr_{0.4}Ba_{0.4}ZrO_3$: A non-equimolar multicomponent perovskite ceramic with low thermal conductivity. *J Eur Ceram Soc* 2020, **40**: 6272–6277.

Just Accepted

[39] Chen L, Li BH, Feng J. Rare-earth tantalates for next-generation thermal barrier coatings. *Prog Mater Sci* 2024, **144**: 101265.

[40] Gan MD, Lu TL, Yu W*, et al.* Capturing and visualizing the phase transition mediated thermal stress of thermal barrier coating materials via a cross-scale integrated computational approach. *J Adv Ceram* 2024, **13**: 413–428.

[41] Xiao WH, Yang Y, Pi ZP*, et al.* Phase stability and mechanical properties of the monoclinic, monoclinic-prime and tetragonal REMO$_4$ (M = Ta, Nb) from first-principles calculations. *Coatings* 2022, **12**: 73.

[42] Lepple M, Ushakov SV, Lilova K*, et al.* Thermochemistry and phase stability of the polymorphs of yttrium tantalate, YTaO$_4$. *J Eur Ceram Soc* 2021, **41**: 1629–1638.

[43] Shannon RD, Prewitt CT. Effective ionic radii in oxides and fluorides. *Acta Cryst B* 1969, **25**: 925–946.

[44] Wang JK, Chen L, Li BH*, et al.* Evolutions of mechanical and thermal properties of TmNbO$_4$/Tm$_3$NbO$_7$ composites as protective coating materials. *J Adv Ceram* 2024, **13**: 1771–1785.

[45] Tian J, Chen L, Chen XL*, et al.* Regulation of crystal and microstructures of RETaO$_4$ (RE = Nd, Sm, Gd, Ho, Er) powders synthesized via co-precipitation. *J Rare Earths* 2025, **43**: 1246–1255.

[46] Schlichting KW, Padture NP, Klemens PG. Thermal conductivity of dense and porous yttria-stabilized zirconia. *J Mater Sci* 2001, **36**: 3003–3010.

[47] Liang YJ, Che YC. *Handbook of Thermodynamic Data of Inorganic Compounds*. Shenyang (China): Northeastern University Press, 1993.

[48] Sanditov DS, Belomestnykh VN. Relation between the parameters of the elasticity theory and averaged bulk modulus of solids. *Tech Phys* 2011, **56**: 1619–1623.

[49] Pandey R, Singh AK. Presence of a monoclinic (Pm) phase in the morphotropic phase boundary region of multiferroic $(1-x)$Bi(Ni$_{1/2}$Ti$_{1/2}$)O$_3$-xPbTiO$_3$ solid solution: A Rietveld study. *J Appl Phys* 2014, **116**: 044102.

Just Accepted

[50] Meng H, Wei P, Tang ZY*, et al.* Data-driven discovery of formation ability descriptors for high-entropy rare-earth monosilicates. *J Materiomics* 2024, **10**: 738–747.

[51] Li BH, Chen L, Hu MY*, et al.* Ferroelastic tetragonal-monoclinic phase transition and anisotropic thermal expansion of $LuNbO_4$ ceramics. *Scr Mater* 2023, **228**: 115258.

[52] Yin BG, Wang L, Mao Ht. Structure-modulated Er^{3+}/Y^{3+} co-doped rare-earth tantalates for upconversion-based optical thermometry in thermal barrier coatings. *Ceram Int* 2026, **52**: 3137–3148.

[53] Robinson K, Gibbs GV, Ribbe PH. Quadratic elongation: a quantitative measure of distortion in coordination polyhedra. *Science* 1971, **172**: 567–570.

[54] Li BH, Wang JK, Chen L*, et al.* Breaking the trade-off relationship between thermal conductivity and toughness of ferroelastic oxide ceramics via a high-density dislocation strategy. *Adv Mater* 2026, **38**: e23083.

[55] Chen L, Wang JK, Li BH*, et al.* Simultaneous manipulations of thermal expansion and conductivity in symbiotic $ScTaO_4/SmTaO_4$ composites via multiscale effects. *J Adv Ceram* 2023, **12**: 1625–1640.

[56] Zhang LY, Chen L, Wang JK*, et al.* High entropy engineering boosts thermo-mechanical properties of rare-earth tantalates: Influences of cocktail effects. *J Materiomics* 2025, **11**: 100984.

[57] Chen L, Hu MY, Wu P*, et al.* Thermal expansion performance and intrinsic lattice thermal conductivity of ferroelastic $RETaO_4$ ceramics. *J Am Ceram Soc* 2019, **102**: 4809–4821.

[58] Liu X, He J, Li Y*, et al.* Foam-gelcasting preparation of porous SiC ceramic for high-temperature thermal insulation and infrared stealth. *Rare Met* 2023, **42**: 3829–3838.

[59] Lai LP, Gan MD, Wang J*, et al.* New class of high-entropy rare-earth niobates with high thermal expansion and oxygen insulation. *J Am Ceram Soc* 2023, **106**: 4343–4357.

[60] Neenu Lekshmi P, da Silva EL, Rocha-Rodrigues P*, et al.* Structural distortions and uniaxial negative thermal expansion in the polar dion–jacobson oxide $RbNdTa_2O_7$. *Chem Mater* 2025, **37**: 5529–5546.

Just Accepted

[61] Zhang FX, Song HQ. Effect of atomic size mismatch and chemical complexity on the local lattice distortion of BCC solid solution alloys. *Mater Today Commun* 2022, **33**: 104367.

[62] Wei XD, An YL, Bu ZY, *et al.* Effect of doping rare earth oxides (RE= Sc, Y, Gd, Eu) on structural, thermal and mechanical properties of $La_2(Zr_{0.7}Ce_{0.3})_2O_7$ ceramics. *Ceram Int* 2023, **49**: 22368–22376.

[63] Wang ZW, Pattamatta ASLS, Jian H, *et al.* Scaling laws for lattice distortions: Application to high entropy alloys. *PNAS Nexus* 2024, **3**: 117.

[64] Liu YW, Fu YM, Gu FC, *et al.* Lattice-distortion-driven reduced lattice thermal conductivity in high-entropy ceramics. *Adv Sci* 2025, **12**: 2501157.

[65] Winiarz P, Sultan A, Ling YH, *et al.* Negative thermal expansion coefficient materials: From basics to applications, recent advances in solid oxide cells and future perspectives. *Sustain Mater Technol* 2025, **45**: e01442.

[66] Wang X, Meng MY, Xu FH, *et al.* $(Lu_{1/7}Yb_{1/7}Sc_{1/7}Er_{1/7}Y_{1/7}Ho_{1/7}Dy_{1/7})_2Si_2O_7$ high entropy rare-earth disilicate with low thermal conductivity and excellent resistance to CMAS corrosion. *J Adv Ceram* 2024, **13**: 549–560.

[67] Liu XY, Zhang P, Huang MZ, *et al.* Effect of lattice distortion in high-entropy $RE_2Si_2O_7$ and RE_2SiO_5 (RE=Ho, Er, Y, Yb, and Sc) on their thermal conductivity: Experimental and molecular dynamic simulation study. *J Eur Ceram Soc* 2023, **43**: 6407–6415.

[68] Yan SS, Wang Y, Tao F, *et al.* High-throughput estimation of phonon thermal conductivity from first-principles calculations of elasticity. *J Phys Chem A* 2022, **126**: 8771–8780.

[69] Callaway J. Model for lattice thermal conductivity at low temperatures. *Phys Rev* 1959, **113**: 1046–1051.

[70] Huang MZ, Liu XY, Zhang P, *et al.* Thermal conductivity modeling on highly disordered crystalline $Y_{1-x}Nb_xO_{1.5+x}$: Beyond the phonon scenario. *Appl Phys Lett* 2021, **118**: 073901.

[71] Liu DB, Shi BL, Geng LY, *et al.* High-entropy rare-earth zirconate ceramics with low thermal conductivity for advanced thermal-barrier coatings. *J Adv Ceram* 2022, **11**: 961–973.

Just Accepted

[72] Yu ZH, Hu DR, Cai FG, *et al.* Phase-structure-dependent thermal and mechanical behavior of high-entropy rare-earth niobates for thermal barrier coating applications. *Mater Today Commun* 2025, **48**: 113637.

[73] Tian Y, Li JX, Zhao XY, *et al.* Improving thermal properties and CMAS corrosion resistance of high entropy rare earth aluminate/zirconate multiphase ceramics as T/EBC materials for Al_2O_{3f}/Al_2O_3 ceramics. *Ceram Int* 2025, **51**: 48688–48699.

[74] Mathew GC, Thomas S. Novel $(La_{0.2}Ce_{0.2}Pr_{0.2}Nd_{0.2}Gd_{0.2})_2Hf_2O_7$ high-entropy pyrochlore oxide as a promising TBC material. *J Eur Ceram Soc* 2025, **45**: 117589.

[75] Wan CL, Pan W, Xu Q, *et al.* Effect of point defects on the thermal transport properties of $(La_xGd_{1-x})_2Zr_2O_7$: Experiment and theoretical model. *Phys Rev B* 2006, **74**: 144109.

[76] Xue GY, Chen L, Wang JK, *et al.* Large atomic displacements act as dominators for reducing thermal conductivity in $Y_{3-x}A_xNbO_7$ (A = Ca, In, Mg, Al; x = 0.05, 0.1) fluorites. *Appl Phys Lett* 2024, **125**: 171902.

[77] Guskov VN, Khoroshilov AV, Ryumin MA, *et al.* Thermal expansion and thermodynamic properties of *M′* -$YbTaO_4$ ceramics. *Ceram Int* 2020, **46**: 5402 – 5406.

[78] Huo JM, Zhong CW, Li EZ, *et al.* New temperature stable $YbTaO_4$ microwave dielectric ceramic with monoclinic structure. *Ceram Int* 2022, **48**: 34465–34471.

[79] Chen L, Hu MY, Wang JK, *et al.* Dominant mechanisms of thermo-mechanical properties of weberite-type RE_3TaO_7 (RE=La, Pr, Nd, Eu, Gd, Dy) tantalates toward multifunctional thermal/environmental barrier coating applications. *Acta Mater* 2024, **270**: 119857.

[80] Zhang YN, Zhu JP, Zou H, *et al.* Effect of lattice distortion on thermal conduction behavior in a novel high-entropy rare-earth tantalates. *J Alloys Compd* 2024, **976**: 172942.

[81] Chen L, Hu MY, Feng J. Defect-dominated phonon scattering processes and thermal transports of ferroelastic $(Sm_{1-X}Yb_X)TaO_4$ solid solutions. *Mater Today Phys* 2023, **35**: 101118.

Just Accepted